Research Article

The Single Septin from *Chlamydomonas reinhardtii* Reveals a Polyproline II Helix-based NC-interface as an Ancestral Scaffold for Filament Assembly

Bryan Marquez [‡], Diego Antonio Leonardo [‡], Eloy Condori, Andressa Alves Pinto, Gabriel Brognara [†], Adriano Alves Furtado, Humberto D'Muniz Pereira, Richard Charles Garratt [*] and Ana Paula U. Araujo [*]

São Carlos Institute of Physics, *USP, São Carlos, SP, Brazil*

Correspondence to Richard Charles Garratt and Ana Paula U. Araujo: *richard@ifsc.usp.br (R.C. Garratt), anapaula@ifsc.usp.br (A.P.U. Araujo)*
https://doi.org/10.1016/j.jmb.2026.169757
Edited by Eric Cascales

Abstract

To date, the most detailed structural characterization of septins has been undertaken on those from opisthokonts, where heterooligomeric complexes polymerize end-to-end into filaments stabilized by alternating G- and NC-interfaces. These filaments are involved in a wide range of essential intracellular processes involving membranes, cytoskeletal components and other binding partners. Their central GTP-binding G-domain is highly conserved and similar to that seen in small monomeric or dimeric GTP-binding proteins, which normally play roles in cell signaling. However, these small GTPases do not polymerize. How and when during evolution septins gained this unique capability is not fully understood. Here we provide seven new crystal structures of the single septin from the green alga, *Chlamydomonas reinhardtii,* in the form of different constructs, mutations, complexes and crystal forms. This has allowed us to describe the unusual properties of the NC-interface for the first time. These include a polyproline II helix in place of the conventional α0 helix, an extension to the first three β-strands, a novel polyacidic region not seen in opisthokonts and a flexible α6 helix whose curvature can vary depending on filament formation or not. This unusual NC-interface may represent a relatively unstable, primordial interaction which has subsequently evolved in opisthokonts to incorporate the more stable α0 helix, an event which occurred in parallel with the gene expansion which enabled the formation of their more robust heterofilaments.

© 2026 The Author(s). Published by Elsevier Ltd. This is an open access article under the CC BY license (http://creativecommons.org/licenses/by/4.0/).

Introduction

Septins are a highly conserved family of cytoskeleton proteins, universally recognized as the "fourth component of the cytoskeleton," complementing actin filaments, microtubules, and intermediate filaments [1]. Their presence spans most eukaryotes. They were initially characterized in *Saccharomyces cerevisiae* [2] and have also been identified in mammals [3], where they form filament-based structures that play roles in cell organization. Recent phylogenetic studies have described their presence in various groups of algae and protists, supporting an ancestral origin for these proteins dating back to the Last Eukaryotic Common Ancestor (LECA) [4].

Functionally, septins self-assemble into non-polar filaments that can adopt bundles or ring-like structures close to the plasma membrane in eukaryotic cells. These polymers fulfill two interrelated roles [5]: the first is as diffusion barriers, limiting the lateral mobility of lipids and proteins to

0022-2836/© 2026 The Author(s). Published by Elsevier Ltd. This is an open access article under the CC BY license (http://creativecommons.org/licenses/by/4.0/).

create functional membrane domains [6], and the second is as molecular scaffolds that recruit regulatory proteins and organize cytoskeletal architecture. Recent research has broadened this perspective, documenting their participation in processes such as cell polarity, morphogenesis, vesicular trafficking, and membrane remodeling [7,8]. They also play a critical role in intracellular bacterial entrapment [9]. Taken together, septins act not as passive structures, but as active elements involved in the integration of cell mechanics, membrane topography and scaffolding within the context of eukaryotic cellular architecture and dynamics.

The functional core of septins resides in the GTPase domain (G-domain), which places them within the P-loop GTPase superfamily. However, unlike canonical signaling GTPases, septins operate at a structural level. Here, guanine nucleotide binding, and in many cases its hydrolysis, directly modulates filament stability and polymerization [10–14]. Filament assembly begins with the longitudinal association of subunits via the G-interface (G-G), mediated by catalytic residues that contribute to dimerization and cooperative GTPase activity [10,11,15]. The NC-interface (N-C) constitutes the second critical point of contact between subunits, essential for determining filament assembly. In Opisthokonta lineages (fungi and animals), this interface stabilizes heterooligomeric complexes (tetramers, hexamers or octamers) and is reinforced by both an α0 helix and a dimeric coiled-coil coming from the N- and C-terminal domains respectively [10,11,16,17].

While evolutionary analyses suggest that the loss of the catalytic arginine finger coincided with septin gene duplication to form heterooligomeric complexes, the green alga *Chlamydomonas reinhardtii* retains the ancestral state [4]. This unicellular organism encodes a single septin (*CrSep*), serving as a simplified and evolutionarily informative model system for studying the possibility of homopolymeric assembly. Previous biophysical characterization revealed that *CrSep* retains the ancestral arginine finger in its G-domain where it reaches across the G-interface to the neighboring nucleotide and allows *CrSep* to act as its own GTPase-activating protein (GAP), thereby accelerating GTP hydrolysis [18]. Although *CrSep* retains the ancestral catalytic machinery for the G-interface, it notably lacks several structural motifs necessary for forming a canonical NC-interface (which is indeed, not observed within the crystal). The most obvious example is the absence of a sequence typical of the α0 helix, a canonical structural element which plays a role in stabilizing the *lower* part of the NC-interface in animal septins [4,17]. Given this observation, it is even more perplexing that critical residues essential for forming the *upper* part of the NC-interface are conspicuously conserved in *CrSep*. Therefore, with what appears to be only a partially canonical NC-interface, a critical question remains: is there an alternative structural mechanism that would allow *CrSep* to stabilize the NC-interface in order to generate homopolymeric filaments such as those observed *in vitro* for the G-domain under low-salt conditions? [18]. Furthermore, how might such an NC-interface shed light on structural aspects of ancestral septins and on the evolution of the family as a whole?

In the present study we have attempted to address this central question using X-ray crystallography to build on our previous report of the G-domain of *CrSep* [18]. In so doing, we have tried to avoid the trap of overinterpreting single X-ray structures by studying a large array of different crystal forms obtained using a variety of constructs, mutants and nucleotide/(AlF_3)-bound complexes in order to provide as complete a picture as possible. We demonstrate, through structures capturing the pre-hydrolytic, transition-state and post-hydrolytic configurations, that *Cr*Sep preserves a fully functional arginine finger-dependent catalytic architecture in the G-domain and, crucially, reveals a possible ancestral mechanism for polymerization. Our results indicate that the α0 helix is functionally replaced by a polyproline type II (PPII) helix, which is enriched in basic residues. This PPII conformation acts as a structural substitute that stabilizes the NC-interface and supports homofilament assembly. Our findings establish an alternative model for filament architecture, offering a key insight into the evolution of septins from simple GTPases toward sophisticated heteropolymeric cytoskeletal complexes.

Results and Discussion

Production and biophysical properties of septin from Chlamydomonas reinhardtii

In a previous study [18], the structure of the *C. reinhardtii* G-domain ($CrSep_G$) was reported but the construct used lacked the N- and C-terminal domains. The asymmetric unit of the crystal contained a G-interface dimer, but the NC-interface was completely absent so that no filaments were observed within the crystal. The N and C-terminal domains (sometimes referred to as the N- and C-terminal extensions) act as stabilizers of this interface. Of particular relevance are the residues which form part of the N-terminal extension prior to the G-domain (the α0 helix and the hook-loop motif), which are fundamental for maintaining the stability of the NC-interface during the oligomerization process [11,19–21].

Thus, with the aim of obtaining a construct that could stabilize and structurally define the NC-interface, AlphaFold3 [22,23] was used to generate a structural model (Figure 1). When four monomers were included in the prediction a tetramer results in which an NC-interface emerges uniting two

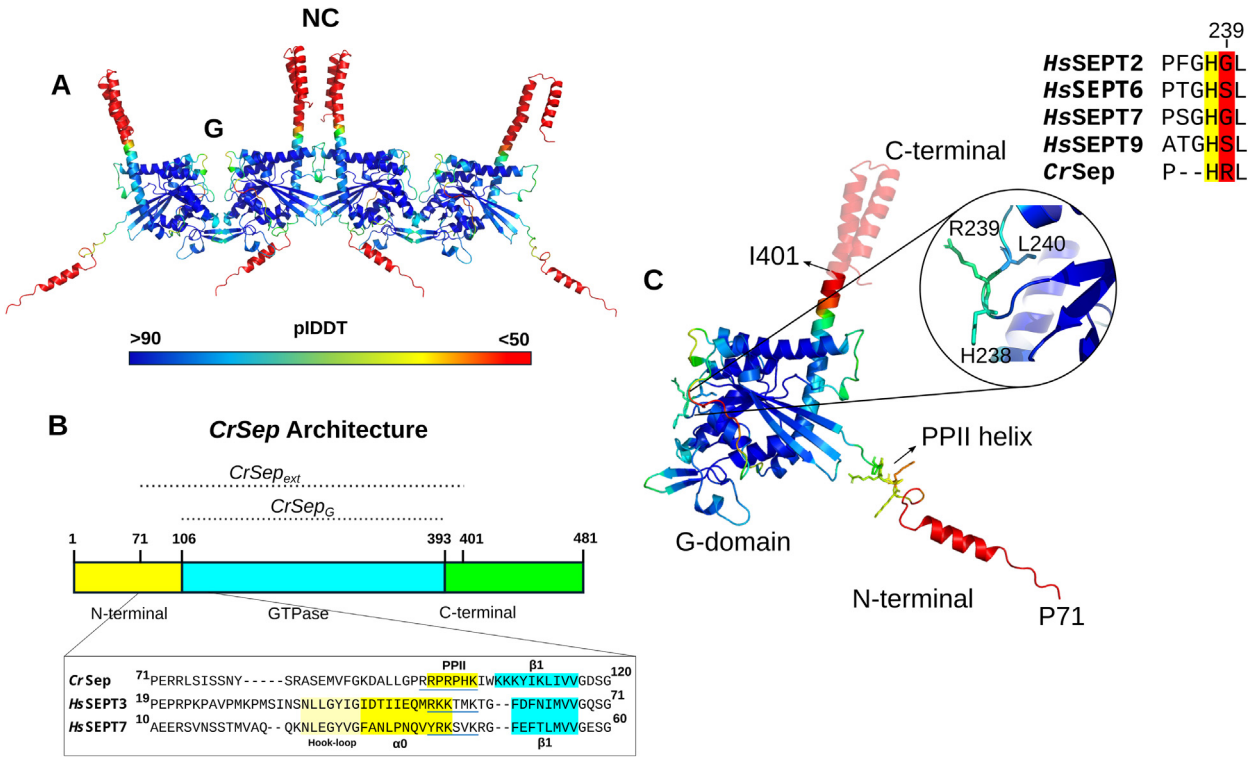

Figure 1. Structural prediction of *C. reinhardtii* septin using AlphaFold3. (A) Homotetrameric model generated for *Cr*Sep showing the canonical interaction interfaces between subunits: the G-interface (including the nucleotide-binding site, as seen in the original crystal structure: 5IRR) and the NC-interface (not observed in 5IRR, but here predicted by AF3). The color gradient (pIDDT) represents the confidence level of the prediction, with blue regions indicating high confidence and red regions indicating low confidence. (B) Schematic representation of the septin monomer displaying its three characteristic domains. A sequence alignment of the *Cr*Sep region (Pro71–Gly120) with human SEPT3 and SEPT7 is shown, highlighting the onset of the β1 strand, the polyproline type-II (PPII) helix in *Cr*Sep, and the α0 motif characteristic of opisthokont septins. The polybasic regions are indicated in a blue line. (C) The final construct used for heterologous expression, comprising residues Pro71–Ile401. This construct includes the central GTPase domain (residues 106–393) together with partial segments of the N-terminal (71–105) and C-terminal (394–401) domains. A structural close-up of the arginine finger region is shown, highlighting R239 in *Cr*Sep together with a sequence comparison demonstrating that this position is occupied by Gly/Ser in opisthokont septins (red background), whereas the preceding histidine (H238) is strictly conserved (yellow background).

G-interface dimers (Figure 1A). Furthermore, this region is of high statistical confidence suggesting that NC-interfaces would be expected to exist *in vivo*, giving rise to the possibility of homofilament formation. The *in silico* analysis suggested that the first 70 residues would be expected to be disordered. Therefore we selected an extended construct spanning residues 71–401 (Figure 1B), which included all the relevant structural elements of the N-terminal domain for NC-interface formation. This encompassed a region which the model predicts to form a polyproline II helix [24,25] in place of α0. In itself this is an interesting observation as AF3 had never seen such a structure in any septin solved to date (Figure 1B and C). The C-terminal domain was largely excluded from the new construct since it is predicted to include a transmembrane region, whose inclusion could compromise solubility and hinder recombinant protein production [18]. This extended construct will be referred to as $CrSep_{71–401}$ or, more simply as $CrSep_{ext}$ to distinguish it from the original G-domain construct ($CrSep_G$).

In the literature, *C. reinhardtii* septin has been described to be that with the highest GTP hydrolysis rate, which is attributed to Arg239, known as the “arginine finger” [4,18]. Sequence alignment with homologous septins from different organisms (*Homo sapiens*, *S. cerevisiae*, and *C. intestinalis*) showed that, at the position equivalent to Arg239, most septins feature a Glycine, but all conserve a Histidine immediately adjacent (Figure 1C). Structural superposition revealed that this His adopts a spatial orientation similar to that of Arg239 in *CrSep*. To evaluate the function of this residue, Arg239 was substituted by Histidine, an amino acid capable of partially mimicking its position and electrostatic properties. Consequently, in addition to the wild-type extended construct ($CrSep_{ext}$), the mutant variant $CrSep_{71–401}$ R239H

was also produced. This will be referred to as R239H$_{ext}$. The wild-type *CrSep*$_G$ and the mutant *CrSep*$_{86–393}$ R239A G-domain (R239A$_G$) constructs were produced as described in Pinto et al. (2017).

CrSep$_{ext}$ and R239H$_{ext}$ were recombinantly produced. Their size-exclusion chromatography (SEC) profiles and analysis by SEC coupled with multi-angle light scattering (SEC-MALS) showed single, well-defined peaks, demonstrating high purity. Furthermore, SEC-MALS confirmed that both proteins existed in a monomeric state in solution (Figure 2A). In addition, nucleotide content analysis by ion-exchange chromatography revealed that *CrSep*$_{ext}$ and R239H$_{ext}$ were both purified as apo proteins, which is compatible with the monomeric state (Figure 2B).

The GTPase activity of both proteins was evaluated by incubating 20 μM of protein with a 10:1 excess of GTP and collecting aliquots at intervals over a total period of 3 h. The added GTP (200 μM) was completely hydrolyzed within 15 min by the wild-type protein (*CrSep*$_{ext}$), demonstrating rapid hydrolysis, as previously described for the G-domain alone (*CrSep*$_G$) [18] (Figure 2C). In contrast, the mutant retained a residual fraction of GTP even after 3 h of incubation, indicating a significant reduction in the hydrolytic rate but without completely abolishing its enzymatic activity altogether (Figure 2C).

The hydrolytic rate of *CrSep*$_{ext}$ was equivalent to that observed for the previous construct, *CrSep*$_G$ [18], indicating that the inclusion of the additional residues at the N- and C-termini did not affect its elevated hydrolytic capacity, which has been attributed to the arginine finger (Arg239) coming from the neighboring subunit where it reaches across the G-interface [4,18,26,27]. Given that *CrSep*$_{ext}$ purifies as a nucleotide-free monomer, its hydrolytic capacity is attributed to the formation of transient G-interfaces in the presence of GTP, where the subunits can act on one another as GAPs, thereby directly accelerating catalysis.

The reduction in hydrolytic capacity of the R239H$_{ext}$ variant was therefore expected. However, this could arise as a consequence of an effect on both interface stability as well as on catalysis itself. Previous analyses of the R239A$_G$ mutant showed the complete abolition of GTPase activity [18]. The R239A$_G$ mutant exhibited a predominantly dimeric state in the presence of GTPγS and a mixture of dimers and monomers in the presence of GDP, with a higher proportion of dimers, indicating the loss of activity to be predominantly an effect on catalysis itself.

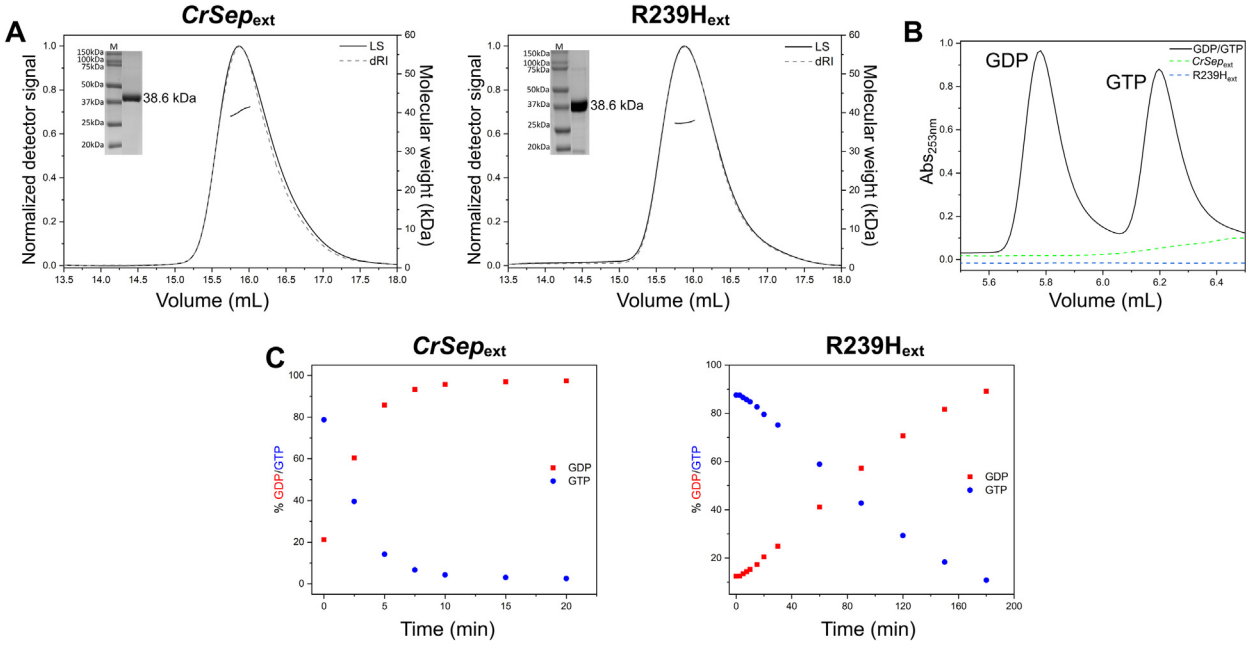

Figure 2. Oligomeric and biophysical characterization of *C. reinhardtii* septin constructs, *CrSep*$_{ext}$ and R239Hext. (A) SEC-MALS chromatograms of CrSep$_{ext}$ and R239H$_{ext}$. Both profiles show that the proteins are monomeric with an apparent mass of approximately 38 kDa, which is consistent with the theoretical value (38.6 kDa). An analysis by 12% SDS-PAGE of the fractions corresponding to the main peak is included as inset (M: molecular weight marker.) (B) Nucleotide content analysis by HPLC for *CrSep*$_{ext}$ (green line) and R239H$_{ext}$ (blue line). Both profiles show no peaks at the retention times corresponding to the GDP and GTP standards (black line), indicating the absence of associated nucleotides. (C) Evaluation of the GTPase activity of CrSep$_{ext}$ and R239H$_{ext}$. The graphs show the hydrolysis of GTP at different incubation times, demonstrating complete hydrolysis in the case of *CrSep*$_{ext}$ after only 15 min and partial hydrolysis in the case of R239H$_{ext}$, with a residual GTP signal even after 3 h.

Taken together, the results indicate that although a single residue (R239) can modulate the rate of hydrolysis, it is not the sole determinant of dimer stability in *C. reinhardtii* septin. Furthermore, the data suggest a close relationship between the catalytic rate, nucleotide retention at the G-interface, and the oligomeric state adopted by the septins, indicating that these processes likely occur concomitantly and in a coordinated manner.

Overall structural architecture and crystal packing of CrSep

The G-domain structure of the *C. reinhardtii* septin ($CrSep_G$) described by Pinto et al. (2017) revealed several distinctive features which may be characteristic of algal septins in general. The presence of an arginine finger (R239) as described above, the extended β1–β2–β3 strands, the absence of the α5′ helix, and a curved α6 helix lacking the α-aneurism (a localized helical distortion previously described in septins that alters the geometry of the helix by the introduction of an additional residue into one of the helical turns) [28] represent its most notable structural characteristics [18]. The α6 helix is part of the "Septin Unique Element (SUE) [29], a sequence of approximately 50 residues which includes important conserved structural elements such as the β-meander [11] and the helices α5 and α6.

However, the ability of *CrSep* to form homofilaments has remained a matter of discussion [4,18], since canonical NC-interfaces were not observed in the crystal lattice (as typically seen in septins from other organisms) [17,21,30,31]. In order to address this issue and to provide additional insight into the catalytic mechanism of *CrSep* we have determined seven crystal structures representing different constructs and ligand-bound states. The first three are based on the G-domain constructs ($CrSep_G$-GppNHp, a non-hydrolysable GTP analog representing the pre-hydrolytic state; $CrSep_G$-GDP/AlF_3, which mimics the γ-phosphate in a transition-state configuration; and $R239A_G$–GDP). A further four are based on the extended constructs bound to GDP ($CrSep_{ext}$-GDP, corresponding to the post-hydrolytic state, and $R239H_{ext}$-GDP). In this case, two different crystal forms were obtained for both the wild-type and the mutant. The structures were refined at resolutions ranging from 2.12 to 2.94 Å (all data collection statistics and quality parameters are summarized in Table 1), revealing that, despite their essentially identical folds, they can exhibit different packing arrangements some of which lead to filament formation via NC-interfaces and others do not (Figure 3).

In general, all structures display the classical αβα septin fold, forming a six-stranded central β-sheet sandwiched between α-helices, and with most regions of the G-domain well defined. However, the degree of order in switch I and in the N-terminal region varies markedly across constructs and correlates with the crystallographic packing mode (Figure 3). The $CrSep_{ext}$ (Figure 3C) and $R239H_{ext}$ (Figure 3E) constructs, which display a zig-zag packing and do not form filaments, contain a single molecule in the asymmetric unit (ASU), and both lack electron density for the first 33 N-terminal residues (positions 71–103) and show a fully disordered switch I (residues 132–144). Despite this disorder, these constructs form a canonical G-interface dimer (upon application of crystallographic symmetry) identical to that observed in the other *CrSep* structures and in septins from other organisms [11,18]. A similar pattern is observed in the $R239A_G$-GDP mutant structure (Figure 3G), which contains two dimers in the ASU where all four subunits exhibit a disordered switch I. In sharp contrast, three of the four crystallographically independent subunits in the two filament forming structures $CrSep_{ext}$-GDP and $R239H_{ext}$ structure, only two residues remain disordered. This is in stark contrast to non-filamentous structures where of the order of 11–12 residues are completely invisible in the electron density map. In summary, in the presence of GDP, there is a strong correlation between the presence of an ordered switch I region and the appearance of normal septin-like filaments within the crystal. Nevertheless, the conformation of the ordered switch I region in these cases is markedly different to that seen in GTP-analog bound structures, as will be discussed below.

Five of the seven structures show a packing arrangement (zig-zag) like that previously reported for $CrSep_G$ [18], exhibiting the canonical G-interface but no NC-interface (Figure 3A–C, E and G). The contacts made between blue and pink dimers in the zig-zag arrangement involve interactions made between β-strands β_1–β_3 and the β-meander, which is distorted in *CrSep* and includes a short α-helix. The $R239A_G$ mutant displays a slightly different lattice organization while still preserving the same canonical G-interface (Figure 3G). None of these arrangements resemble the physiological filaments or pseudo-filamentous assemblies observed in opisthokont septins (summarized in [11]). However, one of the two crystal forms obtained for both $CrSep_{ext}$-GDP (Figure 3D) and $R239H_{ext}$-GDP (Figure 3F) form continuous filaments stabilized by alternating G- and NC-interfaces. In these forms, the N-terminal extension becomes ordered and part of it adopts a polyproline-II (PPII) helix conformation that mediates the NC interaction (see below) and topologically substitutes for the α0 helix observed in opisthokonts. These assemblies constitute the first crystallographic observation of an NC-interface architecture in *Chlamydomonas* that resembles (but is different from) the canonical NC-interfaces described in opisthokont septins, indicating that *CrSep* possesses an intrinsic capacity to polymer-

Table 1 Data-collection and processing statistics.

	CrSep$_G$ – GppNHp	*CrSep$_G$ – AlF$_3$/GDP*	*R239A$_G$ – GDP*	*CrSep$_{ext}$-GDP (non-filament form)*
X-ray source	DLS I04-1	DLS I04-1	DLS I04-1	Sirius MANACA
role="rowhead">Detector	Pilatus 2M	Pilatus 2M	Pilatus 2M	Pilatus 2M
Cell parameters: *a*, *b*, *c* (Å)	178.40, 39.62, 131.09	131.29, 39.31, 163.43	57.05, 83.73, 136.96	54.60, 88.04, 121.84
Cell parameters: α, β, γ (°)	90.0, 118.5, 90.0	90.00, 106.36, 90.00	90.00, 98.75, 90.00	90.0, 90.0, 90.0
Space group	*C*2	*I*2	$P2_1$	$C222_1$
Resolution (Å)	53.94–2.12 (2.18–2.12)	86.97–2.65 (2.78–2.65)	31.95–2.37 (2.43–2.37)	46.40–2.80 (2.95–2.80)
λ (Å)	0.96861	0.96861	0.96861	0.97720
Multiplicity	6.6 (6.8)	12.8 (10.5)	6.7 (6.8)	12.7 (13.2)
R_{pim} (all I+ & I−) (%)	5.6 (56.2)	5.1 (53.3)	7.0 (73.4)	15.7 (68.9)
CC(1/2)	0.996 (0.577)	0.998 (0.644)	0.996 (0.495)	0.988 (0.766)
Completeness (%)	99.9 (100.0)	99.9 (100.0)	99.9 (100.0)	100.00 (100.00)
Reflections	306,002 (23,101)	306,735 (32,960)	349,334 (25,910)	96,140 (14,203)
Unique reflections	46,473 (3420)	23,915 (3145)	51,889 (3805)	7560 (1073)
$\langle I/\sigma(I)\rangle$	8.9 (1.3)	10.1 (1.4)	8.0 (1.2)	7.3 (2.1)
Reflections used in refinement	46,081	23,901	51,859	7534
R (%)*	23.73	25.73	19.28	20.07
R_{free} (%)*	25.38	29.72	24.42	23.00
Number of atoms: protein	4485	4368	8538	2059
Number of atoms: water	182	40	174	11
Number of atoms: ligand	66	66	116	29
B (Å^2)	40.01	63.23	46.46	42.67
Coordinate error (ML-based) (Å)	0.32	0.41	0.39	0.36
Phase error (°)	29.71	36.43	28.65	23.86
Ramachandran favored (%)	96.17	94.96	97.46	98.44
Ramachandran allowed (%)	3.83	4.48	2.45	1.56
All-atom clashscore	2.33	3.88	2.30	2.45
Bond lengths (RMSD) (Å)*	0.002	0.003	0.005	0.002
Bond angles (RMSD) (°)*	0.504	0.624	0.864	0.56
PDB entry	9ZUT	9ZUW	9ZUU	9ZUX

Table 1 (*continued*)

	CrSep$_{ext}$-GDP (filament form)	*R239H$_{ext}$-GDP (non-filament form)*	*R239H$_{ext}$-GDP (filament form)*
X-ray source	DLS VMXm	Sirius MANACA	Sirius MANACA
Detector	Eiger2 XE	Pilatus 2M	Pilatus 2M
Cell parameters: *a*, *b*, *c* (Å)	48.182, 53.649, 76.751	56.64, 85.61, 128.45	45.598, 104.926, 74.030,
Cell parameters: α, β, γ (°)	70.31, 87.83, 84.97	90.00, 90.00, 90.00	90, 91.284, 90
Space group	*P*1	$C222_1$	$P2_1$
Resolution (Å)	72.26–2.59 (2.63–2.59)	47.24–2.94 (3.12–2.94)	42.8–2.50 (2.60–2.50)
λ (Å)	0.610150	0.97720	0.97720
Multiplicity	2.9 (2.86)	13.1 (12.1)	6.8 (7.0)
R_{pim} (all I+ & I−) (%)	–	3.5 (68.2)	12.2 (69.1)
CC(1/2)	0.958 (0.125)	0.999 (0.776)	0.984 (0.582)
Completeness (%)	74.91 (79.16)	100.00 (100.00)	99.12 (98.54)
Reflections	49,424 (2589)	91,525 (13,483)	164,372 (18,833)
Unique reflections	16,812 (904)	6965 (1110)	23,959 (2628)
$\langle I/\sigma(I)\rangle$	6.7 (0.9)	14.1 (1.1)	5.8 (1.2)
Reflections used in refinement	16,181	6870	23,959
R (%)*	24.07	28.93	20.66
R_{free} (%)*	28.48	33.44	24.96
Number of atoms: protein	4440	1841	4806
Number of atoms: water	24	2	129
Number of atoms: ligand	58	29	58
B (Å^2)	55.55	93.56	43.58
Coordinate error (ML-based) (Å)	0.38	0.43	0.38
Phase error (°)	40.49	44.75	28.86
Ramachandran favored (%)	96.24	96.79	96.86
Ramachandran allowed (%)	3.22	2.41	2.64
All-atom clashscore	3.31	2.30	2.20
Bond lengths (RMSD) (Å)*	0.002	0.003	0.004
Bond angles (RMSD) (°)*	0.629	0.568	0.680
PDB entry	9ZV8	9ZV7	9ZUV

* The values in parentheses are from the highest resolution shell. *R is the conventional crystallographic R factor, $\Sigma||Fobs| - |Fcalc|\,|/|Fobs|$, where Fobs and Fcalc are the observed and calculated structure factors respectively. The 5% of the reflections that were excluded from the refinement were used in the Rfree calculation. RMSD, root mean square deviation.*

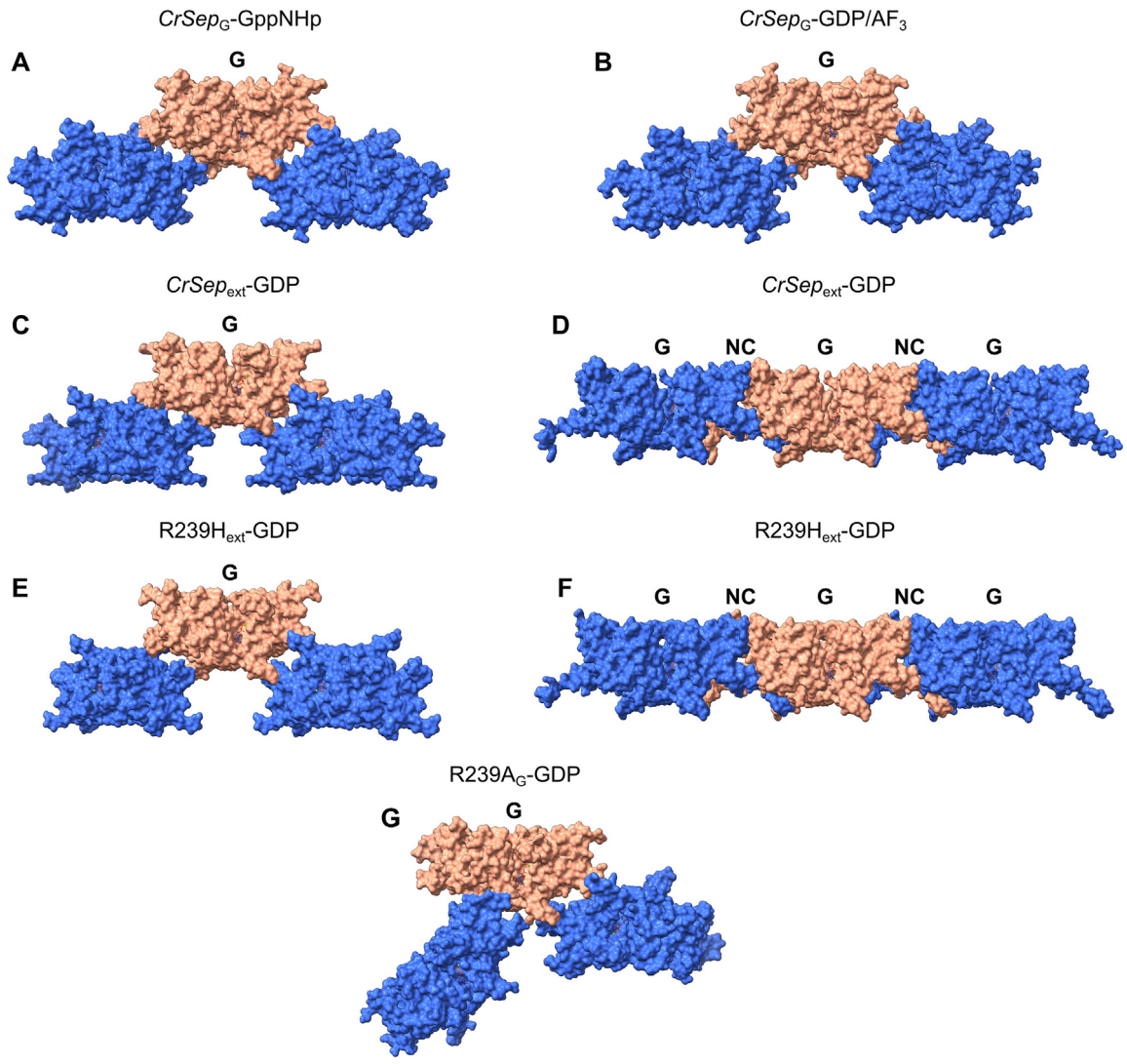

Figure 3. Crystal packing arrangements of *Cr*Sep constructs reveal distinct lattice organizations. All panels show experimentally determined crystal structures expanded by the application of crystallographic symmetry operators. In each case, a reference G-interface homodimer is shown in salmon, while symmetry-related dimers are shown in blue to illustrate the packing environment. Most crystalline forms show the canonical G-interface dimers interacting via crystal contacts, which do not give rise to filaments but rather to a zig-zig arrangement. Only the structures shown in D and F generate filaments via canonical G and NC interfaces within the crystal.

ize provided that the N-terminal region adopts the correct conformation. However, we are unable to categorically affirm, at this stage, that the filaments seen in the crystal are physiological or not.

Our results allow us to explore the hypothesis recently proposed by Delic et al. (2024) [4]: that the G-interface predates the NC-interface in non-opisthokont septins. In all our structures we consistently observe formation of the canonical G-interface, regardless of the construct, the nucleotide bound (either a GTP analog or GDP), or the mutation at the R-finger position. The preferential observation of the G-interface, together with the recurrent absence of a canonical NC-interface in five of the seven crystal forms, supports the proposal by Delic et al. that homodimerization through the G-interface represents an ancestral feature in this group of septins, probably emerging before the establishment of a stable NC contact. Likewise, although the R-finger is essential for accelerated catalytic activity, our structures clearly show that it is not an obligatory requirement for G-interface formation, as both the R239A and R239H mutants still assemble similarly. This finding reinforces the distinction between the catalytic role of the R-finger and the structural determinants governing dimerization and aligns with the view that early septins could form G-dimers even in the absence of efficient catalysis.

In many opisthokont septins, isolated G-domains or single subunits frequently form non-physiological

oligomers through crystal contacts [10,20,32,33]. In *CrSep*, the G-domain alone ($CrSep_G$) has not provided crystallographic evidence for canonical NC-interfaces, as these have not been observed in any of the crystal structures reported to date (Figure 3A, B and G and PDB file 5IRR). Although homofilaments were previously observed by EM [18], the crystal packing arrangements of the isolated G-domain consistently involve lattice-specific contacts rather than NC-interfaces resembling those of opisthokont septins. This is despite possessing residues consistent with polymerization, including those which form conserved salt-bridges at the upper part of the interface [20]. Instead of forming classical G-NC filaments within the crystal lattice, packing consistently occurs through interactions that differ from any previously described septin crystal form and which are unlikely to be of any physiological significance (Figure 3). By contrast, the two filament-forming structures (Figure 3D and F) demonstrate that ordering of the N-terminal region present in the $CrSep_{ext}$ is necessary to stabilize an NC-interface in *Chlamydomonas*. Nevertheless, the same constructs are also capable of showing the zig-zag packing (Figure 3C and E). Interface analysis using PISA indicates that the zigzag contacts bury approximately ~759 Å^2 per interface, substantially less than the ~2564 Å^2 buried in the filament-forming NC-interface. This quantitative difference suggests that the zigzag arrangement likely reflects lattice-driven packing rather than a stable elongated filament, probably indicating that the true NC-interface observed in the filamentous form is less stable than that observed in opisthokonts where NC interfaces are routinely (if not always) observed.

G-interface conformational changes and catalytic mechanism

The nucleotide-dependent conformational changes in the G-domain have been described in some detail for several opisthokont septins, where the nature of the bound nucleotide modulates the orientation of switch I and switch II and, consequently, the G-interface [11,15,17,30]. Comparison of *CrSep* structures bound to GppNHp and GDP (both of which also include Mg^{2+}) reveals that the algal septin exhibits an unusual sensitivity to the nucleotide state, with marked consequences for the conformation of the homodimeric G-interface (Figure 4). In the GppNHp-bound state, $CrSep_G$ adopts a compact conformation, with a 1463 Å^2 buried surface area, in which both switch I and switch II are fully ordered and positioned close to the nucleotide-binding pocket (Figure 4A and C). This pre-hydrolytic arrangement resembles the GTP-bound state of human SEPT3, which also maintains a compact and fully ordered G-interface when bound to GppNHp (Figure 4A). However, even in this fully-ordered state, the classical switch II β-bridge observed in physiological G-interfaces in opisthokonts, is absent in $CrSep_G$ [30,34]. In contrast, different *CrSep* structures bound to GDP exhibit a markedly different behavior. The G-interface becomes noticeably more open, and the degree of switch disorder depends on whether or not the N-terminal extension is ordered and therefore the NC-interface formed. In the $CrSep_{ext}$-GDP structure in which the N-terminal remains disordered (the non-filamentous form), both switches are only partially built, indicating substantial flexibility. This loss of switch order disrupts the upper region of the G-interface (as viewed in Figure 4B), reducing the buried surface area to 894 Å^2 and producing a more open dimer (Figure 4B). This nucleotide-dependent rearrangement is not observed in human SEPT3, where both switches remain ordered in the GDP state, and the G-interface retains a compact configuration (Figure 4B). A distinct conformation of the switch I emerges in the filamentous form of $CrSep_{ext}$-GDP in which the N-terminal extension is ordered (Figure 4D). As mentioned above, in this case switch I is either fully ordered or almost completely so. However, it presents a strikingly different conformation to that seen in the GppNHp-bound form: instead of projecting toward the catalytic site and the G-interface, switch I rotates toward the NC-interface region (Figure 4E and Movie 1). This reorientation contrasts sharply with the pre-hydrolytic state of $CrSep_G$-GppNHp and suggests that switch I may be structurally coupled to NC-interface formation.

The ordered switch II in the filament-forming $R239H_{ext}$-GDP structure provides an excellent opportunity to understand why the *Chlamydomonas* septin fails to form the classical β-bridge at the G-interface, despite retaining some of the key sequence features required for this motif (Figure 5). In opisthokont septins, the β-bridge is a hallmark of the G-interface and is formed by reciprocal hydrogen bonds between the backbone of a conserved Asn/Asp residue located within switch II (Figure 5C) [11]. This interaction stabilizes the upper region of the G-interface and contributes to the compact form observed in human septins, including SEPT3. In the filamentous form of $R239H_{ext}$-GDP, both protomers show a fully ordered switch II (Figure 5A), yet no β-bridge is formed. Furthermore, the sequence alignment in Figure 5B highlights the critical position necessary for forming the β-bridge in opisthokont septins, where D188 in *CrSep* corresponds to the conserved Asn/Asp, confirming that the absence of the β-bridge is not due to sequence divergence but rather reflects a distinct structural arrangement of switch II. Why then, does the β-bridge not form? The explanation appears to be that, immediately after the catalytic threonine (T146) there is an extended segment (E149–E156) which is not present in opisthokont septins (Figure 5B). In both the GppNHp- and GDP-bound states, E149 and R152

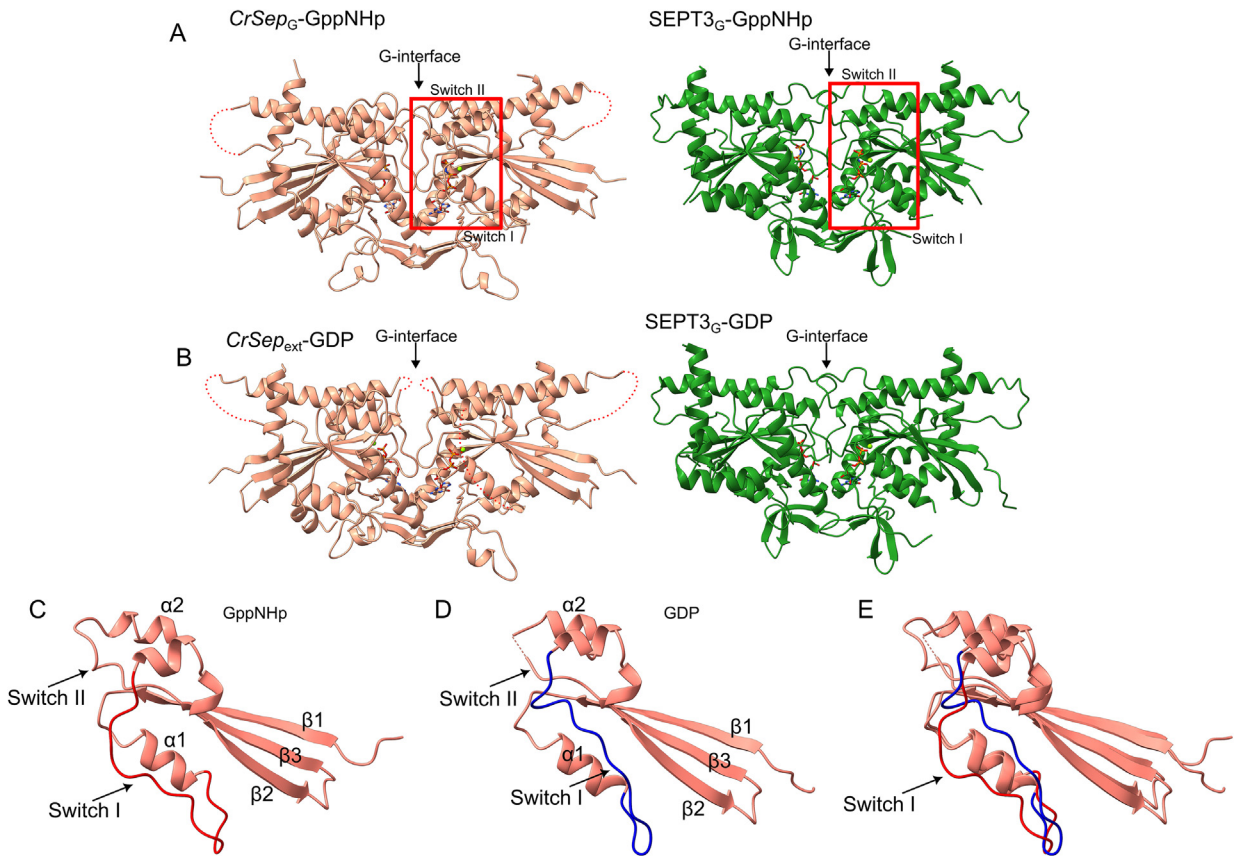

Figure 4. Nucleotide-dependent conformational changes in the *Chlamydomonas reinhardtii* septin (CrSep). (A) Comparison of CrSep$_G$-GppNHp and human SEPT3$_G$-GppNHp (PDB code: 4Z51) [20] showing that both proteins adopt a compact, fully ordered conformation when bound to a GTP-like analog with well-positioned switch I and switch II regions. (B) CrSep$_{ext}$-GDP exhibits an open G-interface relative to SEPT3-GDP (PDB code: 4Z54) [20], reflecting a greater nucleotide-dependent plasticity in CrSep. The figure is taken from the structure of CrSep$_{ext}$-GDP in the non-filamentous form. In both (A) and (B) the arrow indicates the G-interface where two subunits make contact. (C) In the GppNHp-bound state of CrSep$_G$, switch I (shown in red) and switch II are fully ordered and located near the nucleotide-binding pocket. (D) In the CrSep$_{ext}$-GDP structure with an ordered N-terminal extension (the filamentous form), switch I (shown in blue) rotates away from the active site and toward the NC-interface, adopting an orientation distinct from that seen in the GppNHp-bound form. (E) a superposition of (C) and (D).

are electrostatically anchored to E186 and R191 of switch II (which are characteristic of *CrSep*). This leads to reorganization of the switch into an alternative orientation that is incompatible with β-bridge formation potentially leading to a weakened interface (Figure 5C). Although it has been suggested that the presence of the bridge is characteristic of a physiological G-interfaces, our observations on *CrSep* would appear to indicate that this is not universally the case. Furthermore, it is the first indication that, along with the NC-interface, the G-interface may also be more fragile in *CrSep*, implying a final filament which is less robust than those seen in opisthokonts.

The wild-type *CrSep*$_G$ structures solved in three nucleotide-bound states show consecutive steps of the GTPase cycle for an algal septin (Figure 6). In the GppNHp-bound state, the active site adopts a fully competent configuration characteristic of P-loop NTPases [35]. The P-loop residues K123 and T124 coordinate the γ-phosphate and the Mg^{2+}, respectively, while switch I contributes with the catalytic threonine (T146) and switch II with D185, both of which serve to orient the catalytic water. The side chain of R239, from the other subunit, reaches into the active site and interacts with the γ-phosphate, fulfilling the role of the arginine finger (Figure 6A). This arrangement matches the pre-hydrolytic configuration observed in catalytically active opisthokont septins and other P-loop NTPases, in which stimulatory Arg/Lys fingers stabilize the γ-phosphate and prime it for cleavage [35,36]. The GDP/AlF_3-bound structure provides insight into the transition state [37] (Figure 6B). T146 interacts with the AlF_3 and the interaction of H141 from Switch I with the phosphate chain becomes weakened while K123 from the P loop shifts toward the β-phosphate. R239 remains near the catalytic

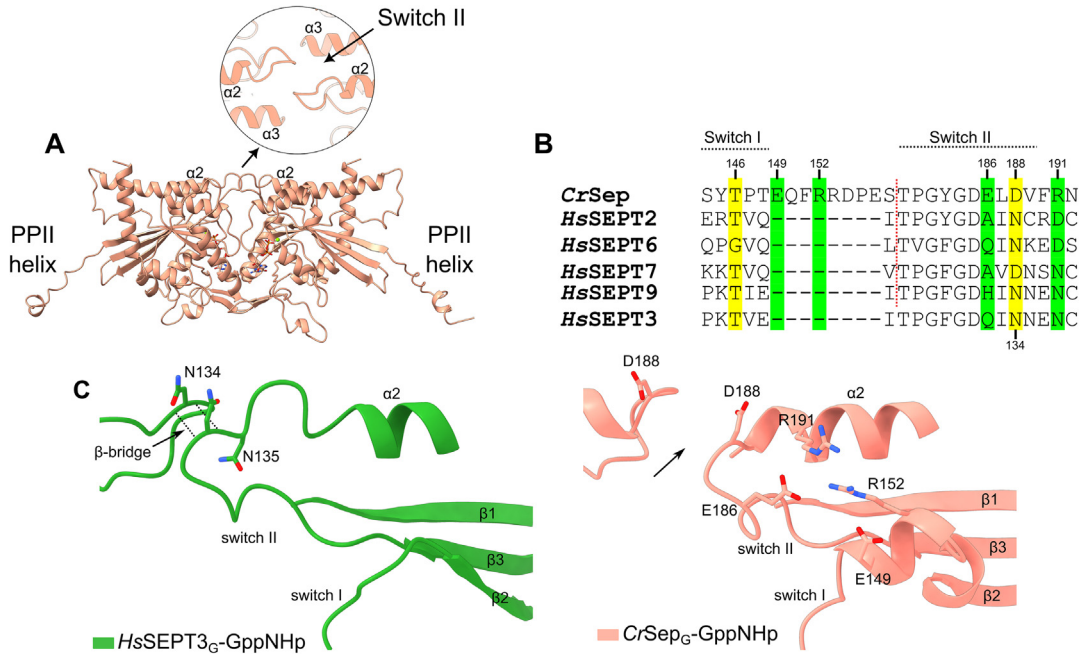

Figure 5. Details of the upper region of the G-interface in CrSep. (A) Overall view of the R239H$_{ext}$-GDP dimer highlighting that both protomers display a fully ordered switch II, yet the characteristic β-bridge observed in opisthokont septins is absent. (B) Sequence alignment of human septins and CrSep showing the conserved residues that form the β-bridge in opisthokonts. The catalytic threonine (T146) and the conserved Asn/Asp residue required for β-bridge formation (D188 in CrSep) are highlighted in yellow in the alignment. The presence of D188 indicates that loss of the β-bridge is not due to sequence divergence. Residues highlighted in green correspond to CrSep characteristic positions implicated in the altered orientation of switch II. The red dotted line indicates a break in the alignment and the residue numbering above the sequences is based on the CrSep sequence. Residue 134, indicated below the alignment refers to SEPT3 as shown in panel C. (C) Structural comparison of human SEPT3 switch II in the GppNHp-bound (PDB code: 4Z51) [20] and CrSep$_G$-GppNHp showing key features that prevent β-bridge formation. The CrSep-specific insertion after T146 (E149–E156), which introduces E149 and R152 and establishes electrostatic contacts with E186 and R191.

center and now interacts with AlF_3. These rearrangements are consistent with a classical in-line nucleophilic attack in which a water molecule (polarized by the T146–D185 pair) attacks the γ-phosphate, while the R-finger stabilizes the accumulating negative charge on the transition state, a catalytic strategy broadly conserved among P-loop NTPases [35]. The GDP-bound structure represents the post-hydrolytic state (Figure 6C) in which the active site has undergone significant rearrangement. In the five different GDP-bound structures presented here the catalytic threonine (T146) and D185 have either moved away from the catalytic center or become completely disordered, precluding their role in orienting the nucleophilic water which, post-hydrolysis, is no longer necessary. In structures with an ordered switch-I, D142 and S144 replace the γ-phosphate and T146 in completing the octahedral coordination sphere of the Mg^{2+} ion. Meanwhile, the intersubunit R-finger (R239) rotates away from the active site and no longer play a role in nucleotide binding. These rearrangements inactivate the catalytic machinery without necessarily requiring switch I disorder (although this does occur in some structures). This indicates that phosphate release drives a coordinated structural relaxation rather than a simple loss of local order. Notably, despite these extensive rearrangements, the G-interface remains intact in the crystal structures, highlighting the robustness of *in crystallo* dimer formation even when the active site adopts a catalytically incompetent geometry. However, this is no guarantee of a similar behavior in solution. Indeed, the data presented in Figure 2 together with that of the original study of Pinto et al. (2017) [18] demonstrate the tendency for both constructs to purify as apo monomers in solution. This indicates the ease with which the nucleotide is lost from the interface, whose fragility may in part be explained by the lack of the β-bridge described above.

Polyproline type II helix (PPII)-based NC-interface reveals an ancestral septin architecture

The *CrSep*$_{ext}$-GDP and R239H$_{ext}$-GDP structures in their filamentous form (Figure 3D and F) provide the most complete and physiologically relevant view

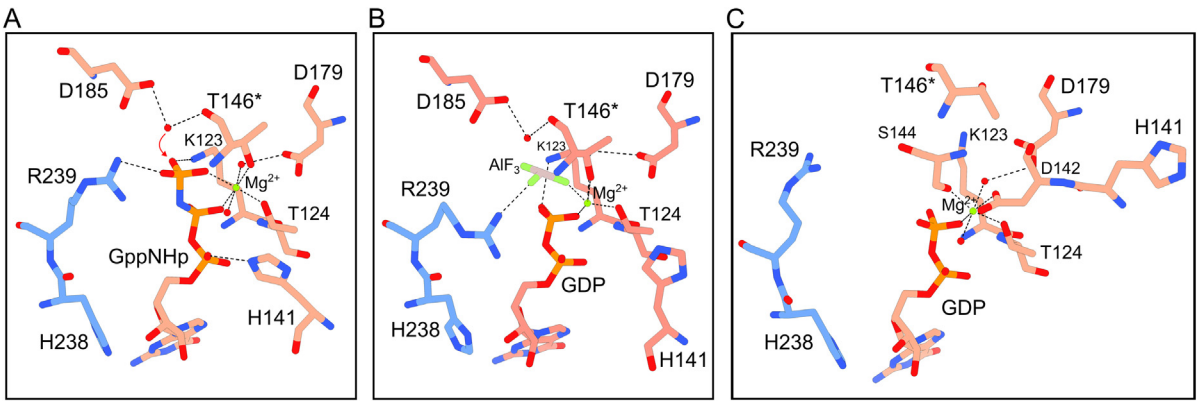

Figure 6. Mechanism of GTP hydrolysis in *CrSep*. (A) Pre-hydrolytic state (*CrSep*$_G$-GppNHp). The active site shows the canonical P-loop NTPase arrangement: K123 and T124 coordinate the γ-phosphate and Mg^{2+}, switch I positions the catalytic threonine T146, and switch II contributes D185 to orient the nucleophilic water. The intersubunit arginine finger R239 engages the γ-phosphate, stabilizing the transition state precursor. (B) Transition-state mimic (*CrSep*$_G$-GDP). Binding of the AlF_3 moiety induces rearrangements typical of a transition state: T146 and H141 uncouple from the phosphate chain, and K123 shifts toward the β-phosphate. R239 weakly interacts with AlF_3, consistent with partial withdrawal of the arginine finger during catalysis. (C) Post-hydrolytic state (*CrSep*$_{ext}$-GDP). Phosphate release triggers a global reorganization of the active site: T146 and D185 move away from the catalytic center, R239 rotates out of the pocket, and D142/S144 partially replace the γ-phosphate and T146 in coordinating Mg^{2+}. Despite this collapse of the catalytic network, the G-interface remains intact, indicating robust dimer stability even after loss of catalytic geometry.

of the heretofore unreported NC-interface in *C. reinhardtii* septin, revealing architectural features unseen before and offering a view into an ancestral mode of polymerization (Figure 7). The structures are well-ordered from around residue 90 onwards and from 99 to 104 the φ/ψ angles are typical of a polyproline type-II (PPII) helix rather than the canonical α0 helix observed in opisthokonts, which encompasses the polybasic (PB1) region (Figure S1 and Figure 7A) [11]. Despite retaining the expected polybasic composition (R99-K104), the unprecedented PPII-helix is more extended and narrower (Figure 7B), positioning *Chlamydomonas* as a structural outlier that may preserve features reminiscent of an ancestral septin architecture. Furthermore, the PPII-helix is composed almost exclusively of prolines and basic residues, and these are highly conserved in all group 6A septins (Figure S2) indicating it to be a relevant structural motif and likely to be a common feature in this subgroup of green algae. It has been reported that PPII helices are relatively common in globular proteins [24,25,38] but these are almost always composed of only three or four residues. Longer examples (such as the six-residue helix described here) are much rarer [24,25]. Beyond collagen, some dramatic examples are to be found in Benzoylformate Decarboxylase [39] and the Obg GTP Binding Protein [40].

The emergence of a PPII-helix correlates with other alterations to the NC-interface. Firstly, there appears to be no correlate of the hook-loop region described for animal septins. This precedes α0 and provides a hydrophobic anchor residue (the HL-residue) which inserts into a binding pocket on the neighboring subunit [11,17]. This anchor has been alternatively described as part of a hydrophobic ridge in *Saccharomyces cerevisiae* [41]. Besides the HL-residue itself, a significant part of the chain prior to α0 embraces the neighboring subunit in a domain-swapped fashion which fastens the two subunits together in animal septins. In the filamentous forms described here there is no equivalent to the HL-residue, nor does domain swapping occur as the region prior to the PPII-helix exits the interface in a completely different direction, incompatible with embracing the neighboring subunit. The absence of these structural features would be expected to significantly weaken the binding of the PPII-helix within the NC-interface cavity. It seems reasonable to assume that it could exit the cavity more readily than α0, thereby providing an easy means by which the polybasic region could become exposed and interact with membranes without requiring the concertina mechanism which has been proposed for SEPT3-group septins [17,20].

A second structural difference is that *CrSep* contains markedly elongated β1–β3 strands that occupy the spatial niche normally partly occupied by α0 in opisthokonts. In *CrSep*, an α-helix (which is wider) would sterically clash with this extended β-sheet, while the narrower PPII-helix fits precisely beneath it, where it docks onto the β-sheet surface (Figure S3). The PPII-helix forms no internal hydrogen bonds and is only tenuously connected with the remainder of the protein as is common for such structures which mostly interact with water molecules [25]. These authors [25] have

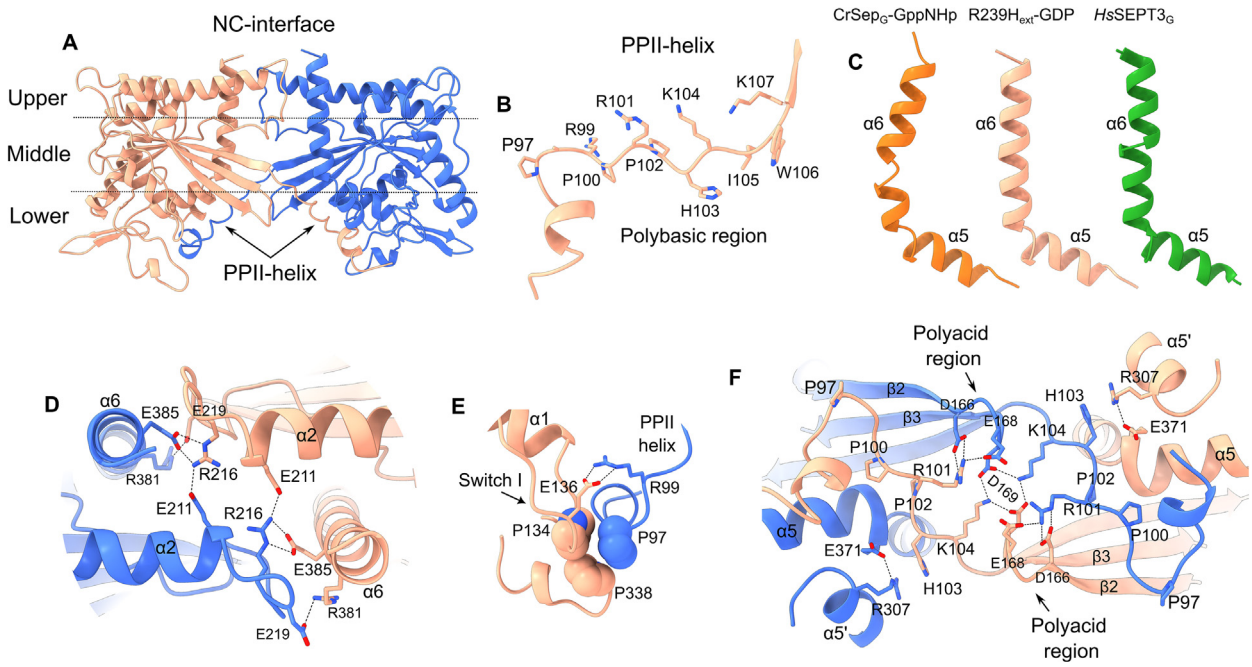

Figure 7. A PPII-helix-based NC-interface reveals an ancestral septin architecture in *Chlamydomonas reinhardtii*. (A) Overall view of the NC-interface formed in the R239H$_{ext}$-GDP structure. The interface is mediated by residues 97–107 of the N-terminal extension, which are fully ordered in both protomers and participate directly in NC docking. The region highlighted in pink indicates the area detailed in panel E. (B) Detail of the N-terminal polyproline type-II (PPII) helix. This segment (P97–K107) contains the polybasic PB1 region (R99–K104), which forms the six-residue PPII helix proper (in red), instead of the α0 helix characteristic of opisthokont septins. (C) The curved α6 helix observed in previously reported CrSep$_G$ structures (and the CrSep$_G$-GppNHp reported here) becomes markedly straighter in both the CrSep$_{ext}$-GDP and R239H$_{ext}$-GDP structures when in their filamentous form, resembling the α6 conformation of human SEPT3. (D) Electrostatic network stabilizing the upper region of the NC-interface. The straightening of α6 is supported by a cluster of salt bridges between α6 and the α2–β4 loop (E211, R216, E219, E385, R381), forming an arrangement analogous to stabilizing networks in upper region of opisthokont NC-interfaces. (E) In the filamentous R239H$_{ext}$-GDP structure, switch I retracts toward the NC-interface and is locked in place by a tri-proline clamp formed by P97, P134 (switch I), and P338 (β-meander), together with an electrostatic contact between R99 (PB1) and E136. Proline residues involved in the clamp are shown as spheres. (F) Divergent architecture of the lower NC-interface. Instead of the canonical α0–α5′ interaction found in opisthokont septins, CrSep employs the PPII PB1 element and an acidic triad in the β2–β3 loop (D166, E168, D169) to establish electrostatic complementarity. This configuration functionally replaces α5′ and the polyacidic regions found in opisthokonts.

suggested that these characteristics of the PPII-helix would allow it to readily transform into other secondary structures such as α-helices, presumably due to the lack of structural restrictions imposed by internal hydrogen bonds. This observation suggests that the α0 helix characteristic of opisthokonts may be a derived feature that replaced a pre-existing PPII as the NC-interface became more compact and stable during septin evolution. What does appear to stabilize the PPII helix within the interface appears to be principally the interaction between Pro97 (prior to its N-terminus) and two further prolines from Switch I and the β-meander (the tri-proline clamp, see below), rather than interactions coming from the main body of the PPII itself.

The previously solved *CrSep*$_G$ structure showed an unusual curvature to helix α6 [18], interpreted as a taxon-specific feature. In the filament-forming R239H$_{ext}$-GDP structure, however, α6 is significantly straighter resembling that of all other structures solved to date (exemplified by human SEPT3 in Figure 7C). However, opisthokont structures, despite being straight, show an α-aneurism in the helix which is absent from *Cr*Sep and the majority of group 6A members, suggesting it to be a feature absent from ancestral septins. This conformational shift is stabilized by an extensive electrostatic network linking α6 to the α2–β4 loop (E211, R216, E219, E385, R381; Figure 7D), an electrostatic network analogous to the salt-bridge clusters that stabilize the upper region of the NC-interfaces in opisthokont septins [11]. The conservation of the charged residues involved and the interactions they make are strong indicators that the NC-interface we describe is indeed physiological and may exhibit similar sensitivity to ionic strength during filament assembly.

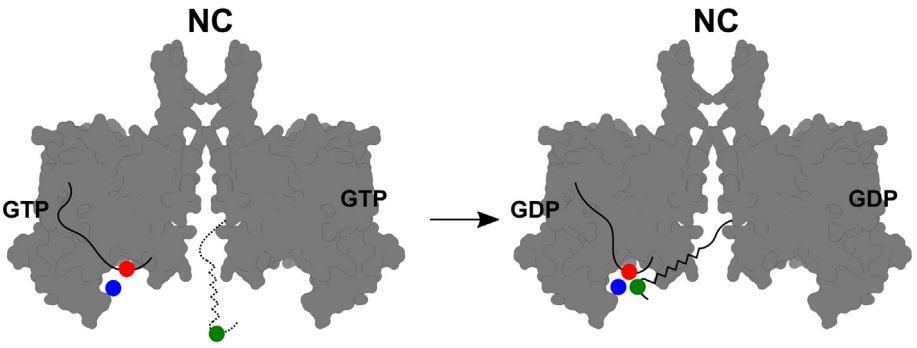

Figure 8. Schematic representation of the structural coupling between the switch I region of one subunit and the PPII helix from the other, across the NC interface. In the GDP bound complex (right) in which an NC interface is formed (and thereby filaments are observed within the crystal) Pro97 (green dot) interacts with Pro134 (red dot) from switch I and Pro338 (blue dot) from the β-meander to form the tri-proline clamp which aids in securing PPII within the interface. In the GTP-bound form (left) switch I (black line) assumes a different conformation to that seen in the GDP-complex and the PPII is exposed and disordered (dotted line).

Figure 7E reveals the mechanistic basis for the unusual orientation of switch I in the filamentous form of R239H$_{ext}$-GDP. In the absence of the γ-phosphate, switch I becomes inherently more flexible, yet in this construct it is stabilized in a retracted orientation directed toward the NC-interface. Three prolines, P97 from the PPII-helix, P134 from switch I, and P338 from the β-meander form a distinctive proline clamp, defined here as a cluster of rigid proline residues whose conformational constraints restrict backbone flexibility and anchor switch I below the NC-interface, while an electrostatic contact between R99 (PPII) and E136 (switch I) further locks it in place. Notably, P338 arises from a *CrSep*-specific insertion that elongates the β-meander relative to opisthokont septins. This clamp explains why there is a strong correlation between the preservation of an ordered switch I region and the presence of an NC-interface in the filamentous structures, as mentioned previously (a schematic mechanism is shown in Figure 8).

It is the lower region of the NC-interface that shows the most remarkable divergence from canonical opisthokont architecture (Figure 7F). In opisthokonts, the polybasic α0 helix interacts with the acidic α5′ helix (the polyacidic region), creating the electrostatic core of the lower region of the NC-interface. *CrSep* lacks both components: α0 is replaced by a PPII-helix, and α5′ is present only as a short remnant that does not contribute to the interface. Instead, *CrSep* repurposes the elongated β-sheet described above to perform a similar role. Specifically, the β-turn which connects β2 and β3 accumulates negative charge due to D166, E168 and D169, expanding it into a functional analog of the canonical α5′ acidic motif. This reorganization preserves electrostatic complementarity but through a radically different structural implementation. The appearance of a novel polyacidic region appears to be necessary because the charge distribution on the PPII-helix will inevitably be different to that on an α-helix due to their different helical parameters. The resulting NC-interface retains the logic of opisthokont interactions while highlighting that the modern α0–α5′ arrangement probably represents a derived, not ancestral, solution to NC-interface stabilization, and particularly the question of how to maintain PB1 buried in the NC-interface when not interacting with membranes.

Overall, the NC-interface buries 2565 Å^2 and contains 34 salt bridge interactions and 35 hydrogen bonds. These values are taken from R239H$_{ext}$-GDP and are comparable to opisthokont septins, such as SEPT9 from *Ciona intestinalis* (2964 Å^2, 24 salt bridges and 48 hydrogen bonds) [17]. This demonstrates that, despite its unconventional architecture, the *CrSep* NC-interface is extensive. Nevertheless, the fact that both *CrSep*$_{ext}$-GDP and R239H$_{ext}$-GDP are able to display both filamentous and non-filamentous behavior (Figure 3C–F) indicates that the NC-interface is likely to be less robust than the canonical form observed in opisthokonts. Furthermore, the surfaces that make up the interface are more plastic and readily molded to suit the two states, as readily exemplified by the dramatic alteration to the curvature of the α6 helix. These findings position the *CrSep* NC-interface as a plausible intermediate which arose during the evolution of septin filaments. We speculate that the filamentous form we observe *in crystallo* (including its novel NC-interface) suggests a mechanism by which filaments could also arise *in vivo.* Nevertheless, it should be appreciated that both interfaces appear to be less stable and filament stabilization *in vivo* may depend on membrane interaction or the presence of other binding partners.

Conclusions

We have provided direct structural observation of an alternative NC-interface found in

Chlamydomonas reinhardtii CrSep which is predicted to be conserved in all group 6A septins. Whilst the upper part of the interface is largely preserved when compared with opisthokont septins, the lower part is dramatically altered to accommodate a polyproline II helix in the space normally occupied by α0. The PPII-helix is composed largely of prolines and basic residues, the latter forming a polybasic region equivalent to that seen in the C-terminal half of α0 in opisthokonts. This alternative helical structure leads to a different spatial distribution of the positive charges and, as a consequence, a novel polyacidic region emerges in the group 6A septins in order to preserve charge neutrality. The classical polyacidic region prior to α5´ in opisthokonts is therefore absent and this is replaced by an acidic cluster coincident with the extended β_2–β_3 sheet strands. The extension of these strands reduces the space available at the interface, which goes hand-in-hand with the narrower PPII-helix when compared with the wider α-helix. Overall, the NC-interface is a combination of a conserved upper region and a radically altered lower region.

The fact that both the wild-type $CrSep_{ext}$-GDP and the mutant R239H$_{ext}$-GDP are able to form the filamentous structure in which the NC-interface is formed (Figure 3D and F) and the zig-zag arrangement (Figure 3C and E) in which it is not, clearly demonstrates that there is intrinsic flexibility to the interface and this is not related to the mutation of the arginine finger. Rather, it would seem that the interface is intrinsically less stable than the canonical form observed in the innumerous opisthokont structures reported to date. Furthermore, the behavior of both the $CrSep_G$ and $CrSep_{ext}$ constructs in solution where they purify as apo monomers, indicates that the G-interface is also probably less robust, probably due to the absence of the β-bridge in its upper region. All of these observations combine to create a picture of a septin which is able to form both G and NC interfaces under appropriate conditions (particularly the high concentrations used for protein crystallization) but which may not be particularly stable *in vivo* where membrane association, the presence of binding partners or post-translational modifications might be essential factors in determining stability. The NC-interface described here may be an evolutionary precursor to the more stable interactions observed in higher organisms which has occurred together with the gene expansion which gave rise to heterofilaments.

Materials and Methods

Cloning, expression and purification

In this work, we express and purify the wild-type $CrSep_{86–393}$ and the mutant $CrSep_{86–393}$ R239A G-domain constructs as described in Pinto et al. (2017). In addition, we designed a DNA coding sequence corresponding to residues 71–401 ($CrSep_{71–401}$) to extend the G-domain in both the N- and C-terminal directions. The N-terminal extension was designed to include the region which could potentially form the α0 helix, important for NC-interface stabilization. We also generated a second catalytic mutant by exchanging the arginine finger for histidine, $CrSep_{71–401}$ R239H. In order to establish a simplified nomenclature for describing the crystal structures, henceforth $CrSep_{86–393}$ will be referred to simply as $CrSep_G$; $CrSep_{71–401}$ as $CrSep_{ext}$; and the mutants as R239A$_G$ and R239H$_{ext}$ in accordance with Table S1. Where necessary the nature of the bound ligands (nucleotide and/or aluminum fluoride – AlF_3) will be added after the name (for example $CrSep_{ext}$-GDP). All crystals obtained (see below) contained Mg^{2+} and, therefore, this will not be explicitly stated in the name of the complex.

The new codon-optimized synthetic CDS genes for expression in *Escherichia coli* were purchased from FastBio (São Paulo, Brazil). Both coding sequences were flanked by *BamH*I and *Hind*III restriction sites and cloned into a modified pET28a expression vector, yielding N-terminal 6XHis-tagged SUMO fusion proteins. For all constructs, expression was carried out in *E. coli* BL21 Rosetta™ (DE3). Cultures were grown in Lysogenic-broth (LB) medium, supplemented with chloramphenicol (34 $\mu g \cdot mL^{-1}$) and kanamycin (50 $\mu g \cdot mL^{-1}$), at 37 °C with shaking at 150 rpm. Protein expression was induced with 0.2 mM IPTG at an A_{600} of 0.6–0.8 and continued at 18 °C for 18 h. Cells were harvested by centrifugation (10,000*g*, 20 min, 4 °C) and resuspended in buffer A (50 mM Tris-HCl pH 7.5, 300 mM NaCl, 5% glycerol, 2 mM $MgCl_2$). Cell lysis was performed by sonication, and the supernatant was clarified by centrifugation (16,000*g*, 45 min, 4 °C). The soluble protein fractions were subjected to immobilized metal affinity chromatography (IMAC) using columns packed with 3 mL of Ni-NTA Superflow resin (Qiagen), previously equilibrated with 10 vol. of buffer A. An initial wash was performed with 10 column vol. of the same buffer, followed by a second wash step using buffer A supplemented with 0.3% Triton X-100. A third wash was then carried out with 10 column volumes of buffer A containing 20 mM imidazole. Recombinant protein was eluted with 5 vol of buffer A supplemented with 250 mM imidazole. To enable cleavage of the SUMO tag, residual imidazole was removed through buffer exchange using a HiPrep 26/10 desalting column (Cytiva). Subsequently, the protein was incubated with SUMO protease at a ratio of 0.2 mg of enzyme per 10 mg of protein sample for 30 min at 10 °C. The resulting mixture was subjected to a second IMAC step to remove the SUMO tag, which remained bound to the resin,

thereby allowing recovery of the target protein in its purified form. The purified protein was then aliquoted into 1 mL fractions and stored at −80 °C. All steps of the procedure were performed at a constant temperature of 10 °C. The final purification step was performed by size-exclusion chromatography (SEC) on a Superdex 75 10/300 GL column (GE Healthcare) connected to an ÄKTA Purifier system (GE Healthcare), equilibrated with buffer B (15 mM Hepes pH 7.5, 300 mM NaCl, 5% glycerol, 2 mM $MgCl_2$). Fractions from all purification steps were analyzed by 12% SDS-PAGE.

Size exclusion chromatography coupled with multi-angle light scattering (SEC-MALS)

The polydispersity, oligomeric state and the influence of nucleotide on the latter were determined for the different constructs by size-exclusion chromatography coupled with multi-angle light scattering, using a miniDAWN® TREOS® light-scattering detector and an Optilab T-REX differential refractometer (Wyatt Technology). The system was integrated with an HPLC (Shimadzu model LC-2030C 3D). A 50 μL sample (2.5 mg/mL) was injected into a Superdex 200 Increase 10/300 GL column (Cytiva) equilibrated with buffer containing 25 mM Hepes (pH 7.5), 300 mM NaCl, and 5 mM $MgCl_2$. Data acquisition and analysis were performed using ASTRA 7 software (Wyatt Technology).

Nucleotide binding and hydrolytic activity assay

To assess the presence and nature of endogenous bound nucleotides, soluble proteins were adjusted to 20 μM in 50 mM Tris–HCl buffer (pH 7.5) containing 150 mM NaCl, 5% (v/v) glycerol, and 2 mM $MgCl_2$, and subjected to thermal denaturation at 100 °C for 10 min to release associated nucleotides. Precipitated proteins were removed by centrifugation at 11,200*g* for 10 min at 4 °C. The supernatant containing the released nucleotides was transferred to 600 μL tubes and stored at −80 °C prior to analysis.

Nucleotide detection was performed by ion-exchange chromatography using an HPLC system equipped with a Protein-Pak DEAE-5 PW column (10 μm, 7.5 mm × 7.5 cm; Waters™) connected to a Shimadzu model LC-2030C 3D HPLC module. The column was equilibrated with 25 mM Tris–HCl buffer (pH 7.5). A 200 μL sample was injected, and nucleotides were eluted with a linear NaCl gradient (0.1–0.45 M over 10 min). As controls, 20 μM GDP and GTP solutions prepared in the same buffer were analyzed under identical conditions and the absorbance was monitored at 253 nm.

For GTP hydrolysis analysis, proteins (initially apo) were adjusted to 20 μM and GTP was added to a final concentration of 200 μM. After nucleotide addition, aliquots were collected at intervals of time. Samples were frozen, subsequently heat-denatured, and the supernatant was analyzed by HPLC according to the procedure described in the nucleotide identification section.

Crystallization, data collection and structure determination

In this paper we report on seven different crystal structures. Alternative *CrSep* constructs were crystallized in the presence of different ligands (5 mM GppNHp, 5 mM GDP and 2 mM Mg^{2+}) by the sitting drop vapor diffusion method, using the Morpheus I, Morpheus II and SG1™ kits (Molecular Dimensions). To analyze the transition state of GTP hydrolysis to GDP, aluminum fluoride (AlF_3), a reagent widely used in studies of the hydrolytic mechanism of NTPase, was employed. Aluminum fluoride was generated by preparing a stock solution consisting of 0.1 M $AlCl_3$ and 1 M NaF, from which a final concentration of 2 mM was used for co-crystallization experiments. A drop of 0.2 μL of each sample (2.5 mg mL^{-1} of pure protein) was mixed with 0.2 μL of stock solution and incubated at 291 K. After 2–5 days, crystals were obtained under different conditions as described in the Table S2. The harvested crystals were cryo-cooled in liquid nitrogen for data collection.

X-ray diffraction data of $CrSep_{ext}$-GDP and $R239H_{ext}$-GDP (two different crystal forms) were obtained at the MANACÁ beamline of the Sirius synchrotron (*Laboratório Nacional de Luz Síncrotron – Centro Nacional de Pesquisa em Energia e Materiais – LNLS-CNPEM, Campinas, Brazil*) using a PILATUS 2M detector. The data for $CrSep_G$-GppNHp, $CrSep_G$-GDP/AF_3 and $R239A_G$-GDP were collected at beamline I04-1 with a PILATUS 2M detector at the Diamond Light Source (Didcot, United Kingdom). Indexing, integration, and scaling were performed with autoPROC [42]. The $CrSep_G$ constructs were solved by molecular replacement using Phaser [43], with the previously reported structure by Pinto et al. 2017 (PDB ID: 5IRR) used as the search model. For the extended constructs, including both native and mutant forms, an AlphaFold-predicted structure was employed as the search model. Model refinement and building were carried out using alternating cycles of phenix.refine [44] and Coot [45]. A second dataset for the $CrSep_{ext}$-GDP construct was collected from microcrystals on beamline VMXm using an Eiger2X 9M detector at the Diamond Light Source (Didcot, United Kingdom). Indexing, integration, and scaling were performed using xia2.multiplex [46]. Molecular replacement was carried out with MOLREP [47] using an AlphaFold-predicted structure as the search model. Model refinement and building were carried out as described above.

Figures were generated with UCSF ChimeraX 1.10.1 [48]. Data collection and refinement statistics, as well as PDB codes, are presented in Table S3.

Accession numbers

The data underlying this article are available in the UniProt (accession number A8IYS5·A8IYS5_CHLRE) and Protein Data Bank (PDB identifiers 9ZUT, 9ZUW, 9ZUU, 9ZUX, 9ZV8, 9ZV7, 9ZUV).

CRediT authorship contribution statement

Bryan Marquez: Writing – original draft, Validation, Methodology, Investigation, Formal analysis, Data curation. **Diego Antonio Leonardo:** Writing – review & editing, Writing – original draft, Validation, Methodology, Investigation, Formal analysis, Data curation, Conceptualization. **Eloy Condori:** Writing – original draft, Validation, Methodology, Investigation, Formal analysis, Data curation. **Andressa Alves Pinto:** Validation, Methodology, Investigation, Formal analysis, Data curation. **Gabriel Brognara:** Validation, Methodology, Investigation, Formal analysis, Data curation. **Adriano Alves Furtado:** Validation, Methodology, Investigation, Formal analysis, Data curation. **Humberto D'Muniz Pereira:** Validation, Methodology, Investigation, Formal analysis, Data curation. **Richard Charles Garratt:** Writing – review & editing, Writing – original draft, Supervision, Resources, Project administration, Funding acquisition, Conceptualization. **Ana Paula U. Araujo:** Writing – review & editing, Writing – original draft, Supervision, Resources, Project administration, Funding acquisition, Conceptualization.

DATA AVAILABILITY

The data underlying this article are publicly available in UniProt (accession number A8IY55; A8IY55_CHLRE) and in the Protein Data Bank (PDB identifiers 9ZUT, 9ZUW, 9ZUU, 9ZUX, 9ZV8, 9ZV7, 9ZUV).

DECLARATION OF COMPETING INTEREST

All the authors declare that they have no conflicts of interest in relation to this work.

Acknowledgments

We gratefully acknowledge the support of the São Paulo Research Foundation (FAPESP) via thematic grant 2020/02897-1. A.P.U.A (304852/2021-0), B.M (132173/2023-9) and A.A.F (141503/2023-8) received scholarships from the Conselho Nacional de Desenvolvimento Científico e Tecnológico – Brasil (CNPq), D.A.L. (2021/08158-9) from FAPESP and E.C (8887.820519/2023-00) from Coordenação de Aperfeiçoamento de Pessoal de Nível Superior – Brasil (CAPES). We acknowledge the Diamond Light Source (DLS) for access to beamlines I04-1 and VMXm under project proposals nt14493-77 and MX43121-2. We are particularly grateful to the beamline staff for their excellent technical support throughout all stages of data collection. We thank Adam Crawshaw and Anna Warren from the VMXm beamline for their essential assistance and expertise. We acknowledge the Brazilian Synchrotron Light Laboratory (LNLS), part of the Brazilian Center for Research in Energy and Materials (CNPEM), a private non-profit organization under the supervision of the Brazilian Ministry for Science, Technology, and Innovation (MCTI). The Manacá beamline staff is acknowledged for assistance during the diffraction data collection experiments (project proposal 20240851 and 20252511).

Appendix A. Supplementary material

Supplementary material to this article can be found online at https://doi.org/10.1016/j.jmb.2026.169757.

Received 30 December 2025;
Accepted 11 March 2026;
Available online 17 March 2026

Keywords:
algae septins;
Chlamydomonas reinhardtii;
poly-proline helix;
NC-interface;
X-ray crystallography

† Current Address: Vienna Bioscience Core Facility, Campus Vienna Biocenter 1, 1030 Vienna, Austria.
‡ These authors contributed equally to this work.

References

[1]. Mostowy, S., Cossart, P., (2012). Septins: the fourth component of the cytoskeleton. *Nature Rev. Mol. Cell Biol.* **13**, 183–194. https://doi.org/10.1038/nrm3284.

[2]. Hartwell, L.H., (1971). Genetic control of the cell division cycle in yeast: IV. Genes controlling bud emergence and cytokinesis. *Exp. Cell Res.* **69**, 265–276. https://doi.org/10.1016/0014-4827(71)90223-0.

[3]. Kinoshita, M., Kumar, S., Mizoguchi, A., Ide, C., Kinoshita, A., Haraguchi, T., Hiraoka, Y., Noda, M., (1997). Nedd5, a mammalian septin, is a novel cytoskeletal component interacting with actin-based structures. *Genes Dev.* **11**, 1535–1547 https://genesdev.cshlp.org/content/11/12/1535.abstract.

[4]. Delic, S., Shuman, B., Lee, S., Bahmanyar, S., Momany, M., Onishi, M., (2024). The evolutionary origins and ancestral features of septins. *Front. Cell Dev. Biol.* **12** https://doi.org/10.3389/fcell.2024.1406966.

[5]. Bridges, A.A., Gladfelter, A.S., (2015). Septin form and function at the cell cortex. *J. Biol. Chem.* **290**, 17173–17180. https://doi.org/10.1074/jbc.R114.634444.

[6]. Caudron, F., Barral, Y., (2009). Septins and the lateral compartmentalization of eukaryotic membranes. *Dev. Cell* **16**, 493–506. https://doi.org/10.1016/j.devcel.2009.04.003.

[7]. Benoit, B., Poüs, C., Baillet, A., (2023). Septins as membrane influencers: direct play or in association with other cytoskeleton partners. *Front. Cell Dev. Biol.* **11** https://doi.org/10.3389/fcell.2023.1112319.

[8]. Das, A., Kunwar, A., Septins,, (2024). Structural insights, functional dynamics, and implications in health and disease. *J. Cell Biochem.*e30660. https://doi.org/10.1002/jcb.30660.

[9]. Robertin, S., Mostowy, S., (2020). The history of septin biology and bacterial infection. *Cell. Microbiol.* **22**, e13173. https://doi.org/10.1111/cmi.13173.

[10]. Sirajuddin, M., Farkasovsky, M., Hauer, F., Kühlmann, D., Macara, I.G., Weyand, M., Stark, H., Wittinghofer, A., (2007). Structural insight into filament formation by mammalian septins. *Nature* **449**, 311–317. https://doi.org/10.1038/nature06052.

[11]. Cavini, I.A., Leonardo, D.A., Rosa, H.V.D., Castro, D.K.S.V., D'Muniz Pereira, H., Valadares, N.F., Araujo, A.P.U., Garratt, R.C., (2021). The structural biology of septins and their filaments: an update. *Front. Cell Dev. Biol.* **9** https://doi.org/10.3389/fcell.2021.765085.

[12]. Mendoza, M., Hyman, A.A., Glotzer, M., (2002). GTP binding induces filament assembly of a recombinant septin. *Curr. Biol.* **12**, 1858–1863. https://doi.org/10.1016/S0960-9822(02)01258-7.

[13]. Farkasovsky, M., Herter, P., Voss, B., Wittinghofer, A., (2005). Nucleotide binding and filament assembly of recombinant yeast septin complexes. *Biol. Chem.* **386**, 643–656. https://doi.org/10.1515/BC.2005.075.

[14]. Field, C.M., Al-Awar, O., Rosenblatt, J., Wong, M.L., Alberts, B., Mitchison, T.J., (1996). A purified Drosophila septin complex forms filaments and exhibits GTPase activity. *J. Cell Biol.* **133**, 605–616. https://doi.org/10.1083/jcb.133.3.605.

[15]. Sirajuddin, M., Farkasovsky, M., Zent, E., Wittinghofer, A., (2009). GTP-induced conformational changes in septins and implications for function. *PNAS* **106**, 16592–16597. https://doi.org/10.1073/pnas.0902858106.

[16]. Sala, F.A., Valadares, N.F., Macedo, J.N.A., Borges, J.C., Garratt, R.C., (2016). Heterotypic coiled-coil formation is essential for the correct assembly of the septin heterofilament. *Biophys. J.* **111**, 2608–2619. https://doi.org/10.1016/j.bpj.2016.10.032.

[17]. Mendonça, D.C., Morais, S.T.B., Ciol, H., Pinto, A.P.A., Leonardo, D.A., D'Muniz Pereira, H., Valadares, N.F., Portugal, R.V., Klaholz, B.P., Garratt, R.C., Araujo, A.P.U., (2024). Structural insights into ciona intestinalis septins: complexes suggest a mechanism for nucleotide-dependent interfacial cross-talk. *J. Mol. Biol.*168693. https://doi.org/10.1016/j.jmb.2024.168693.

[18]. Pinto, A.P.A., Pereira, H.M., Zeraik, A.E., Ciol, H., Ferreira, F.M., Brandão-Neto, J., DeMarco, R., Navarro, M.V.A.S., Risi, C., Galkin, V.E., Garratt, R.C., Araujo, A.P.U., (2017). Filaments and fingers: novel structural aspects of the single septin from *Chlamydomonas reinhardtii*. *J. Biol. Chem.* **292**, 10899–10911. https://doi.org/10.1074/jbc.M116.762229.

[19]. Barral, Y., Kinoshita, M., (2008). Structural insights shed light onto septin assemblies and function. *Curr. Opin. Cell Biol.* **20**, 12–18. https://doi.org/10.1016/j.ceb.2007.12.001.

[20]. Castro, D.K.S. do V., da Silva, S.M. de O., Pereira, H.D., Macedo, J.N.A., Leonardo, D.A., Valadares, N.F., Kumagai, P.S., Brandão-Neto, J., Araújo, A.P.U., Garratt, R.C., (2020). A complete compendium of crystal structures for the human SEPT3 subgroup reveals functional plasticity at a specific septin interface. *IUCrJ* **7**, 462–479. https://doi.org/10.1107/S2052252520002973.

[21]. Marques da Silva, R., Christe dos Reis Saladino, G., Antonio Leonardo, D., D'Muniz Pereira, H., Andréa Sculaccio, S., Paula Ulian Araujo, A., Charles Garratt, R., (2023). A key piece of the puzzle: the central tetramer of the *Saccharomyces cerevisiae* septin protofilament and its implications for self-assembly. *J. Struct. Biol.* **215**, 107983. https://doi.org/10.1016/j.jsb.2023.107983.

[22]. Jumper, J., Evans, R., Pritzel, A., Green, T., Figurnov, M., Ronneberger, O., Tunyasuvunakool, K., Bates, R., Žídek, A., Potapenko, A., Bridgland, A., Meyer, C., Kohl, S.A.A., Ballard, A.J., Cowie, A., Romera-Paredes, B., Nikolov, S., Jain, R., Adler, J., Back, T., Petersen, S., Reiman, D., Clancy, E., Zielinski, M., Steinegger, M., Pacholska, M., Berghammer, T., Bodenstein, S., Silver, D., Vinyals, O., Senior, A.W., Kavukcuoglu, K., Kohli, P., Hassabis, D., (2021). Highly accurate protein structure prediction with AlphaFold. *Nature* **596**, 583–589. https://doi.org/10.1038/s41586-021-03819-2.

[23]. Abramson, J., Adler, J., Dunger, J., Evans, R., Green, T., Pritzel, A., Ronneberger, O., Willmore, L., Ballard, A.J., Bambrick, J., Bodenstein, S.W., Evans, D.A., Hung, C.-C., O'Neill, M., Reiman, D., Tunyasuvunakool, K., Wu, Z., Žemgulytė, A., Arvaniti, E., Beattie, C., Bertolli, O., Bridgland, A., Cherepanov, A., Congreve, M., Cowen-Rivers, A.I., Cowie, A., Figurnov, M., Fuchs, F.B., Gladman, H., Jain, R., Khan, Y.A., Low, C.M.R., Perlin, K., Potapenko, A., Savy, P., Singh, S., Stecula, A., Thillaisundaram, A., Tong, C., Yakneen, S., Zhong, E.D., Zielinski, M., Žídek, A., Bapst, V., Kohli, P., Jaderberg, M., Hassabis, D., Jumper, J.M., (2024). Accurate structure prediction of biomolecular interactions with AlphaFold 3. *Nature* **630**, 493–500. https://doi.org/10.1038/s41586-024-07487-w.

[24]. Kumar, P., Bansal, M., (2016). Structural and functional analyses of PolyProline-II helices in globular proteins. *J. Struct. Biol.* **196**, 414–425. https://doi.org/10.1016/j.jsb.2016.09.006.

[25]. Adzhubei, A.A., Sternberg, M.J.E., (1993). Left-handed Polyproline II helices commonly occur in globular proteins. *J. Mol. Biol.* **229**, 472–493. https://doi.org/10.1006/jmbi.1993.1047.

[26]. Koenig, P., Oreb, M., Höfle, A., Kaltofen, S., Rippe, K., Sinning, I., Schleiff, E., Tews, I., (2008). The GTPase cycle of the chloroplast import receptors Toc33/Toc34: implications from monomeric and dimeric structures. *Structure* **16**, 585–596. https://doi.org/10.1016/j.str.2008.01.008.

[27]. Schwefel, D., Arasu, B.S., Marino, S.F., Lamprecht, B., Köchert, K., Rosenbaum, E., Eichhorst, J., Wiesner, B., Behlke, J., Rocks, O., Mathas, S., Daumke, O., (2013). Structural insights into the mechanism of GTPase activation in the GIMAP family. *Structure* **21**, 550–559. https://doi.org/10.1016/j.str.2013.01.014.

[28]. Keefe, L.J., Sondek, J., Shortle, D., Lattman, E.E., (1993). The alpha aneurism: a structural motif revealed in an insertion mutant of staphylococcal nuclease. *PNAS* **90**, 3275–3279. https://doi.org/10.1073/pnas.90.8.3275.

[29]. Versele, M., Gullbrand, B., Shulewitz, M.J., Cid, V.J., Bahmanyar, S., Chen, R.E., Barth, P., Alber, T., Thorner, J., (2004). Protein–protein interactions governing septin heteropentamer assembly and septin filament organization in *Saccharomyces cerevisiae*. *Mol. Biol. Cell* **15**, 4568–4583. https://doi.org/10.1091/mbc.e04-04-0330.

[30]. Rosa, H.V.D., Leonardo, D.A., Brognara, G., Brandão-Neto, J., D'Muniz Pereira, H., Araújo, A.P.U., Garratt, R. C., (2020). Molecular recognition at septin interfaces: the switches hold the key. *J Mol Biol 432*, 5784–5801. https://doi.org/10.1016/j.jmb.2020.09.001.

[31]. de Freitas Fernandes, A., Leonardo, D.A., Cavini, I.A., Rosa, H.V.D., Vargas, J.A., D'Muniz Pereira, H., Nascimento, A.S., Garratt, R.C., (2022). Conservation and divergence of the G-interfaces of *Drosophila melanogaster* septins. *Cytoskeleton*. https://doi.org/10.1002/cm.21740.

[32]. Brognara, G., Pereira, H.D.M., Brandão-Neto, J., Araujo, A.P.U., Garratt, R.C., (2019). Revisiting SEPT7 and the slippage of β-strands in the septin family. *J. Struct. Biol.* **207**, 67–73. https://doi.org/10.1016/j.jsb.2019.04.015.

[33]. Zeraik, A.E., Pereira, H.M., Santos, Y.V., Brandão-Neto, J., Spoerner, M., Santos, M.S., Colnago, L.A., Garratt, R. C., Araújo, A.P.U., DeMarco, R., (2014). Crystal structure of a *Schistosoma mansoni* septin reveals the phenomenon of strand slippage in septins dependent on the nature of the bound nucleotide. *J. Biol. Chem.* **289**, 7799–7811. https://doi.org/10.1074/jbc.M113.525352.

[34]. Grupp, B., Graser, J.B., Seifermann, J., Gerhardt, S., Lemkul, J.A., Gehrke, J.F., Johnsson, N., Gronemeyer, T., (2025). Interface integrity in septin protofilaments is maintained by an arginine residue conserved from yeast to man. *Mol. Biol. Cell* **36**, ar59. https://doi.org/10.1091/mbc.E25-01-0041.

[35]. Kozlova, M.I., Shalaeva, D.N., Dibrova, D.V., Mulkidjanian, A.Y., (2022). Common mechanism of activated catalysis in P-loop fold nucleoside triphosphatases—united in diversity. *Biomolecules* **12** https://doi.org/10.3390/biom12101346.

[36]. Ahmadian, M.R., Stege, P., Scheffzek, K., Wittinghofer, A., (1997). Confirmation of the arginine-finger hypothesis for the GAP-stimulated GTP-hydrolysis reaction of Ras. *Nature Struct. Biol.* **4**, 686–689. https://doi.org/10.1038/nsb0997-686.

[37]. Xu, Y.-W., Moréra, S., Janin, J., Cherfils, J., (1997). AlF3 mimics the transition state of protein phosphorylation in the crystal structure of nucleoside diphosphate kinase and MgADP. *PNAS* **94**, 3579–3583. https://doi.org/10.1073/pnas.94.8.3579.

[38]. Sreerama, N., Woody, R.W., (1994). Poly(Pro)II helixes in globular proteins: identification and circular dichroic analysis. *Biochemistry* **33**, 10022–10025. https://doi.org/10.1021/bi00199a028.

[39]. Hasson, M.S., Muscate, A., McLeish, M.J., Polovnikova, L.S., Gerlt, J.A., Kenyon, G.L., Petsko, G.A., Ringe, D., (1998). The crystal structure of benzoylformate decarboxylase at 1.6 Å resolution: diversity of catalytic residues in thiamin diphosphate-dependent enzymes. *Biochemistry* **37**, 9918–9930. https://doi.org/10.1021/bi973047e.

[40]. Buglino, J., Shen, V., Hakimian, P., Lima, C.D., (2002). Structural and biochemical analysis of the Obg GTP binding protein. *Structure* **10**, 1581–1592. https://doi.org/10.1016/S0969-2126(02)00882-1.

[41]. Grupp, B., Denkhaus, L., Gerhardt, S., Vögele, M., Johnsson, N., Gronemeyer, T., (2024). The structure of a tetrameric septin complex reveals a hydrophobic element essential for NC-interface integrity. *Commun. Biol.* **7**, 48. https://doi.org/10.1038/s42003-023-05734-w.

[42]. Vonrhein, C., Tickle, I.J., Flensburg, C., Keller, P., Paciorek, W., Sharff, A., Bricogne, G., (2018). Advances in automated data analysis and processing within autoPROC, combined with improved characterisation, mitigation and visualisation of the anisotropy of diffraction limits using STARANISO. *Acta Crystallogr. A* **74**, a360. https://doi.org/10.1107/S010876731809640X.

[43]. McCoy, A.J., Grosse-Kunstleve, R.W., Adams, P.D., Winn, M.D., Storoni, L.C., Read, R.J., (2007). {\it Phaser} crystallographic software. *J. Appl. Crystallogr.* **40**, 658–674. https://doi.org/10.1107/S0021889807021206.

[44]. Adams, P.D., Afonine, P.V., Bunkóczi, G., Chen, V.B., Davis, I.W., Echols, N., Headd, J.J., Hung, L.-W., Kapral, G.J., Grosse-Kunstleve, R.W., McCoy, A.J., Moriarty, N. W., Oeffner, R., Read, R.J., Richardson, D.C., Richardson, J.S., Terwilliger, T.C., Zwart, P.H., (2010). {\it PHENIX}: a comprehensive Python-based system for macromolecular structure solution. *Acta Crystallogr. Sect. D* **66**, 213–221. https://doi.org/10.1107/S0907444909052925.

[45]. Emsley, P., Cowtan, K., (2004). {\it Coot}: model-building tools for molecular graphics. *Acta Crystallogr. Sect. D* **60**, 2126–2132. https://doi.org/10.1107/S0907444904019158.

[46]. Gildea, R.J., Beilsten-Edmands, J., Axford, D., Horrell, S., Aller, P., Sandy, J., Sanchez-Weatherby, J., Owen, C.D., Lukacik, P., Strain-Damerell, C., Owen, R.L., Walsh, M. A., Winter, G., (2022). xia2. multiplex: a multi-crystal data-analysis pipeline. *Acta Crystallogr. Sect. D* **78**, 752–769. https://doi.org/10.1107/S2059798322004399.

[47]. Vagin, A., Teplyakov, A., (1997). {\it MOLREP}: an automated program for molecular replacement. *J. Appl. Crystallogr.* **30**, 1022–1025. https://doi.org/10.1107/S0021889897006766.

[48]. Meng, E.C., Goddard, T.D., Pettersen, E.F., Couch, G.S., Pearson, Z.J., Morris, J.H., Ferrin, T.E., (2023). U.C.S.F. ChimeraX: tools for structure building and analysis. *Protein Sci.* **32**, e4792. https://doi.org/10.1002/pro.4792.